A Born Type Iterative Method for Imaging of Heterogeneous Scattering Media and Its Application to Simulated Breast Tissue

Yuqi Yao*, Yaling Pei*, Yao Wang* and Randall L. Barbour‡

* Polytechnic University, Brooklyn, NY 11201

‡ SUNY Health Science Center, Brooklyn, NY 11203

Abstract

In this paper, we present a Born-Type iterative algorithm for reconstruction of absorption and diffusion coefficient distributions of a heterogeneous scattering medium. This method is derived based on the integral form of the diffusion equation for the photon flux. It takes into account the nonlinear nature of the problem by using an iterative perturbation approach. Within each iteration, the forward problem (update of the total field and Green's function) is solved by the finite element method (FEM), and the inverse problem (update of the medium properties) is obtained by a regularized least squares method. This method has been used to reconstruct "pathologies" embedded in an inhomogeneous test medium simulating a normal female breast from frequency domain data. The test medium is constructed by assigning optical coefficients according to a MR derived anatomical map. Our simulation results show that the algorithm is computationally practical and can yield qualitatively and quantitatively correct absorption and scattering distributions of embedded objects from simulated data with up to 5% additive noise in the simulated measurement data.

Keywords: optical imaging, image reconstruction, Born approximation, inverse scattering, diffusion model, finite element method, CGD method

1. Introduction

In this paper, we present a Born-Type iterative algorithm for reconstruction of absorption and diffusion coefficient distributions of a heterogeneous scattering medium. This method is derived based on the integral form of the diffusion equation for the photon flux. The Born-type iterative method is used for reconstruction of human tissue based on MR-derived anatomical maps. The algorithm is based on the minimization of an error norm describing the difference between measured data and calculated data with a forward model from the previous reconstruction of the distribution of the optical properties. The approach takes into account the nonlinear nature of the problem, and updates both the total field and Green's function based on the previous reconstruction, until the error norm is sufficiently small. The forward problem (update of the total field and Green's function) is solved by the finite element method (FEM) [13], which can handle arbitrary physical boundary. The inverse problem (solution of the perturbation equation) is solved by a regularized conjugate gradient descent (CGD) method. Some numerical experiments have been conducted using test media derived from MR images. These are obtained by computing solutions to the forward problem for segmented 2-D MR data sets in which the identified tissue types have been assigned optical properties. In this manner we can easily simulate a measurement using a model that is anatomically accurate, and for which we can vary the contrast, size, and number of simulated pathologies in relation to a range of properties of the background tissue.

2. Integral Equation and Solution by FEM

The diffusion equation for the photon density u in a bounded region Ω is given by:

$$\nabla \cdot [D(\mathbf{r})\nabla u(\mathbf{r})] + (-\mu_a(\mathbf{r}) + i\frac{\omega}{v})u(\mathbf{r}) = -S(\mathbf{r}), \quad \mathbf{r} \in \Omega \tag{1}$$

SPIE Vol. 2979 • 0277-786X/97/$10.00

where $\mu_a(\mathbf{r})$ and $D(\mathbf{r})$ represent the absorption coefficient and diffusion coefficient respectively, $S(\mathbf{r})$ represents the source distribution, ω is the modulation frequency, and v is the speed of light. The photon density u in Eq. (1) is subject to the boundary condition:

$$u = u_0 \quad \text{on } \Omega_s \tag{2}$$

where Ω_s is the surface of Ω, and u_0 specifies a Dirichlet boundary condition on this surface. The output photon flux on Ω_s is given by:

$$J(\mathbf{r}) = -D(\mathbf{r})\hat{\mathbf{n}} \cdot \nabla u(\mathbf{r})|_{\Omega_s}, \tag{3}$$

where $\hat{\mathbf{n}}(\mathbf{r})$ is the unit normal vector of Ω_s.

Consider the actual medium as a perturbation of a background medium with absorption and diffusion coefficients described by $\mu_a^b(\mathbf{r})$ and $D_b(\mathbf{r})$, respectively. Then the position-dependent incremental changes in the optical properties with respect to the background are defined by

$$\delta\mu_a(\mathbf{r}) = \mu_a(\mathbf{r}) - \mu_a^b(\mathbf{r}), \quad \delta D(\mathbf{r}) = D(\mathbf{r}) - D_b(\mathbf{r}). \tag{4}$$

Let

$$u_s(\mathbf{r}) = u(\mathbf{r}) - u_b(\mathbf{r}) \tag{5}$$

be the difference (perturbation) between the total field $u(\mathbf{r})$ for the actual medium and the background field $u_b(\mathbf{r})$ generated by the same source illumination. By inserting Eq. (4) into Eq. (1) in such a way as to isolate the terms corresponding to the background in the left-hand side, and those corresponding to the perturbation in the right-hand side, we obtain

$$\nabla \cdot [D_b(\mathbf{r})\nabla u(\mathbf{r})] + (-\mu_a^b(\mathbf{r}) + i\frac{\omega}{v})u(\mathbf{r}) = -S(\mathbf{r}) - f_s(\mathbf{r}), \tag{6}$$

where

$$f_s(\mathbf{r}) = \nabla \cdot [\delta D(\mathbf{r})\nabla u(\mathbf{r})] - \delta\mu_a(\mathbf{r})u(\mathbf{r}) \tag{7}$$

is referred to as the secondary source function. From Eq. (6), we can derive the following volume integral equation for the scattered field (*i.e.* the perturbation field) of photon density [14]

$$u_s(\mathbf{r}) = -\int_\Omega \delta\mu_a(\mathbf{r}')u(\mathbf{r}')G(\mathbf{r},\mathbf{r}')d\mathbf{r}' - \int_\Omega \delta D(\mathbf{r}')\nabla' u(\mathbf{r}') \cdot \nabla' G(\mathbf{r},\mathbf{r}')d\mathbf{r}'. \tag{8}$$

The scattered field of photon flux on the surface of tissue can be obtained from Eq. (3).

In this report, we assume that the flux is measured on the boundary. The finite element method is adopted to solve Eq. (1) with the boundary condition described in Eq. (2) to obtain the solution of the forward problem [12]. To derive the perturbation equation for the inverse problem, let N and M denote the total numbers of nodes and elements, L the number of the nodes on the boundary, d the number of detectors for each source, s the number of sources, and Ω_m the region of the j^{th} element. The perturbation of output flux vector $\delta\mathbf{J}^{(p)}$ at detector locations $(\xi_1, \xi_2, \cdots, \xi_d)$ for p^{th} source configuration can be expressed as

$$\delta\mathbf{J}^{(p)} = \mathbf{T}\ \delta\mathbf{u}^{(p)}, \tag{9}$$

where, T is a $d \times (N - L)$ transformation matrix, which can be derived from Eq. (3) using the FEM technique, and $[\delta\mathbf{u}^{(p)}]^T = [\delta u_1^{(p)}\ \delta u_2^{(p)} \cdots \delta u_k^{(p)} \cdots \delta u_{N-L}^{(p)}]$ is the interior nodal field perturbation vector due to perturbations δD and $\delta\mu_a$ for the P^{th} source. Assume that there exists a constant change of δD and $\delta\mu_a$ within each element, then we have

$$\delta u_k^{(p)} = -\sum_{j=1}^{M}(\delta\mu_a)_j \int_{\Omega_j} u^{(p)}(\mathbf{r}')G(\mathbf{r}_k,\mathbf{r}')d\mathbf{r}' - \sum_{j=1}^{M}(\delta D)_j \int_{\Omega_j} \nabla u^{(p)}(\mathbf{r}') \cdot \nabla G(\mathbf{r}_k,\mathbf{r}')d\mathbf{r}'. \tag{10}$$

Note that $\delta u_k^{(p)}$ is the perturbation at the k^{th} interior node due to the p^{th} source. We can rewrite $\delta\mathbf{u}^{(p)}$ in a matrix notation:

$$\delta\mathbf{u}^{(p)} = [\mathbf{B}_D^{(p)}\ \mathbf{B}_{\mu_a}^{(p)}]\ \mathbf{x}, \tag{11}$$

where $\mathbf{x} = [\delta D_1\ \delta D_2\ \cdots \delta D_M\ \delta\mu_{a,1}\ \delta\mu_{a,2}\ \cdots\ \delta\mu_{a,M}]$. The entries of $\mathbf{B}_D^{(p)}$ and $\mathbf{B}_{\mu_a}^{(p)}$ are found from Eq. (10) to be

$$(B_D^{(p)})_{kj} = -\int_{\Omega_j} \nabla u^{(p)}(\mathbf{r}') \cdot \nabla G(\mathbf{r}_k, \mathbf{r}') d\Omega, \quad (B_{\mu_a}^{(p)})_{kj} = -\int_{\Omega_j} u^{(p)}(\mathbf{r}') \cdot G(\mathbf{r}_k, \mathbf{r}') d\Omega. \tag{12}$$

Substituting Eq. (11) into Eq. (9), Eq. (9) becomes:

$$\delta\mathbf{J}^{(p)} = \mathbf{T}\ [\mathbf{B}_D^{(p)}\ \mathbf{B}_{\mu_a}^{(p)}]\mathbf{x} = [\mathbf{W}_D^{(p)}\ \ \mathbf{W}_{\mu_a}^{(p)}]\mathbf{x} = \mathbf{W}^{(p)}\mathbf{x}, \tag{13}$$

where

$$\mathbf{W}_D^{(p)} = \mathbf{T}\ \mathbf{B}_D^{(p)}, \quad \mathbf{W}_{\mu_a}^{(p)} = \mathbf{T}\ \mathbf{B}_{\mu_a}^{(p)} \tag{14}$$

A complete perturbation equation can be obtained for all sources as:

$$\delta\mathbf{J} = \mathbf{W}\mathbf{x}, \tag{15}$$

where

$$\mathbf{W} = \begin{bmatrix} \mathbf{W}^{(1)} \\ \cdot \\ \cdot \\ \cdot \\ \mathbf{W}^{(s)} \end{bmatrix}, \quad \delta\mathbf{J} = \begin{bmatrix} \delta\mathbf{J}^{(1)} \\ \cdot \\ \cdot \\ \cdot \\ \delta\mathbf{J}^{(s)} \end{bmatrix}. \tag{16}$$

The matrix $\mathbf{W}$ is called the weight matrix. In fact, it is unnecessary to compute all $\delta u_k^{(p)}$ because only those $\delta u_k^{(p)}$ connected to detector locations contribute to $\delta\mathbf{J}^{(p)}$. For the complete weight matrix, only $s + \alpha \times d$ FEM runs are required, where α is the number of nodes connecting with each detector location which depends on the type of element and the generated mesh used in the FEM solution. For 2-D cases using linear triangular elments, α is usually a value equal to or less than 3.

3. Implementation of the Born-Type Iterative Method

Equation (15) can be rewritten as follows

$$\mathbf{W}_{\mu_a} \cdot \delta\mu_\mathbf{a} + \mathbf{W}_\mathbf{D} \cdot \delta\mathbf{D} = \delta\mathbf{J}, \tag{17}$$

In frequency-domain, $\mathbf{W}_{\mu_a}$, $\mathbf{W}_\mathbf{D}$ and $\mathbf{J}_\mathbf{s}$ are complex variables. If we define $\mathbf{W}_{\mu_a} = \mathbf{W}_{\mu_a}^{(R)} + i\mathbf{W}_{\mu_a}^{(I)}$, $\mathbf{W}_D = \mathbf{W}_D^{(R)} + i\mathbf{W}_D^{(I)}$, and $\delta\mathbf{J} = \delta\mathbf{J}^{(R)} + i\delta\mathbf{J}^{(I)}$, then Eq. (17) equivalent to

$$\begin{bmatrix} \mathbf{W}_{\mu_a}^{(R)} & \mathbf{W}_D^{(R)} \\ \mathbf{W}_{\mu_a}^{(I)} & \mathbf{W}_D^{(I)} \end{bmatrix} \begin{bmatrix} \delta\mu_\mathbf{a} \\ \delta\mathbf{D} \end{bmatrix} = \begin{bmatrix} \delta\mathbf{J}^{(R)} \\ \delta\mathbf{J}^{(I)} \end{bmatrix}. \tag{18}$$

To find $\delta\mu_\mathbf{a}$ and $\delta\mathbf{D}$ (or $\mathbf{x}$) via a regularized minimization, we note that the regularization has to be performed with respect to two unknowns. Denoting the $\delta\mu_\mathbf{a}$ and $\delta\mathbf{D}$ regularization matrices by $\mathbf{R_1}$ and $\mathbf{R_2}$, respectively, the problem of finding $\delta\mu_\mathbf{a}$ and $\delta\mathbf{D}$ can be posed as follows: find $\delta\mu_\mathbf{a}$ and $\delta\mathbf{D}$ (or $\mathbf{x}$) such that the norm $||\delta\mathbf{J} - \mathbf{W} \cdot \mathbf{x}||^2$ is minimized, subject to the constraint that $||\mathbf{R_1} \cdot \delta\mu_\mathbf{a}||^2$ and $||\mathbf{R_2} \cdot \delta\mathbf{D}||^2$ are also minimized. In other words, we need to solve an optimization problem which minimizes the functional

$$I(\mathbf{x}) = ||\delta\mathbf{J} - \mathbf{W} \cdot \mathbf{x}||^2 + \gamma_1||\mathbf{R_1} \cdot \delta\mu_\mathbf{a}||^2 + \gamma_2||\mathbf{R_2} \cdot \delta\mathbf{D}||^2. \tag{19}$$

The two scalars γ_1 and γ_2 are regularization parameters. Assuming $\mathbf{R_1}$ and $\mathbf{R_2}$ to be identity matrices, then $\delta\mu_\mathbf{a}$ and $\delta\mathbf{D}$ can be found from the matrix equation

$$\mathbf{W}^* \cdot \mathbf{W} \cdot \mathbf{x} + \gamma \cdot \mathbf{x} = \mathbf{W}^* \cdot \delta\mathbf{J} \tag{20}$$

where * denotes conjugate transpose, and γ is a diagonal matrix given by

$$\gamma = \begin{bmatrix} \gamma_1 \mathbf{I} & 0 \\ 0 & \gamma_2 \mathbf{I} \end{bmatrix}. \tag{21}$$

We now summarize this algorithm as follows:

(i) Set $[\mathbf{p}^{(0)}]^T = [\mu_a{}^{(0)}\ \mathbf{D}^{(0)}]$ to be initial guess of the distribution of the optical parameters in the tissue, then calculate $\mathbf{u}_b^{(0)}$, $\mathbf{J}_b^{(0)}$, and $\delta\mathbf{J}^{(0)} = \mathbf{J}^m - \mathbf{J}_b^{(0)}$, and derive $\mathbf{W}^{(0)}$ using the technique described in section 2. Here $\mathbf{J}^m$ denotes measured flux data at detector locations.

(ii) Find $\mathbf{x}^{(n)}$ by solving

$$\mathbf{W}^{*(n)} \cdot \mathbf{W}^{(n)} \cdot \mathbf{x}^{(n)} + \gamma \cdot \mathbf{x}^{(n)} = \mathbf{W}^{*(n)} \cdot \delta\mathbf{J}^{(n)}$$

(iii) Calculate

$$r^{(n)} = \sqrt{\frac{\sum_{j=1}^{N} [x_j^{(n)}]^2}{\sum_{j=1}^{N} [p_j^{(n)}]^2}},$$

where N is the total number of the unknowns. If $r^{(n)} > \epsilon$, set $\mathbf{p}^{(n+1)} = \mathbf{x}^{(n)} + \mathbf{p}^{(n)}$, then determine $\mathbf{J}_b^{(n+1)}$ and $\mathbf{W}^{(n+1)}$ based on $\mathbf{p}^{(n+1)}$, and calculate $\delta\mathbf{J}^{(n+1)} = \mathbf{J}^m - \mathbf{J}_b^{(n+1)}$, and go to (ii), else stop.

4. Reconstruction of Test Media Simulating Female Breast Tissues

In this section, we show the reconstruction results on the simulated female breast containing "added pathologies". The optical properties in the medium are derived based on anatomic maps obtained from 2-D magnetic resonance images (MRI). Segmentation of the breast data was achieved using a thresholding method followed by identifying and deleting isolated regions [15].

4.1 Setting up the Background Medium from MR Data

The basic approach we use is to perform a series of MR measurements on the breast of a volunteer, segment the resulting images according to tissue types, assign estimates of the optical properties to the background tissues, and introduce "virtual tumors" to selected areas. The resulting data set becomes the starting point for the computation of optical tomographic data.

Specifically, in the studies conducted here a series of 24 MR breast images of a volunteer were obtained using a GE MR system. The fast spin echo(TR = 400 ms, TE = 112 ms, 3-mm thickness) technique was used, with and without fat and water saturation. Surface coils were used, to obtain better uniformity of the field. Image data were collected with the subject lying prone in the magnet, which caused some degree of dorsal-ventral compression of the breast. This series of sagittal sections was then segmented into two different tissue types: (i) fat and (ii) parenchyma. The segmentation was done by a simple thresholding technique; all MR image pixels with image intensities ≤ 128 were assumed to be fat and all those > 128 were assumed to be parenchyma.

Figure 1 shows four sagittal sections $(5^{th}, 10^{th}, 15^{th}, 20^{th})$ of the MR data set, which are for slices that are perpendicular to the chest wall. Fig. 2 shows the image of absorption coefficient and diffusion coefficient distributions in an axial slice in which two "pathologies" have been introduced by assigning different absorption and scattering coefficient values to two small regions. Table 1 lists the values of optical properties assigned to different tissue types and added tumors.

In our implementation we used the Dirichlet boundary condition $u(\mathbf{r}) = 0$ on the physical boundary Ω_s, and 10 point sources are evenly placed at a position $d \cong 1/\mu_s'$ below the physical boundary. The 10 detectors are uniformly spread on the physical boundary.

Table 1: Optical Properties Assigned to Different Tissue Types in the Simulated Female Breast (in cm^{-1})

Fat		Parenchyma		Tumor 1		Tumor 2	
μ_a	μ_s'	μ_a	μ_s'	μ_a	μ_s'	μ_a	μ_s'
0.04	10.0	0.08	7.0	0.15	20.0	0.20	15.0

4.2 Reconstruction Results

Here, we show reconstructed images of the absorption and diffusion coefficient distributions without and with noise for a 2-D axial slice. Here, The measurements consist of 100 source-detector pairs, while the medium is divided into 1800 elements with a total of 1800×2 unknowns. Therefore the problem is severly underdetermined. Each of the two objects has a radius approximately 0.5 cm, and separated by 2.5 cm. The optical properties of the two objects are different as listed in Table 1.

Figure 3 shows the spatial distribution of the true absorption coefficient, of the object and those of the reconstructed profiles after the indicated number of iterations. The target profile is shown in Fig. 3(a). Fig. 3(b) shows the result obtained with the first-order Born approximation. Fig. 3(c) shows the reconstruction result after 20 iterations. Similarly, Fig. 4 shows the spatial distributions of the diffusion coefficient, of the true object and those of the reconstructed profiles after the indicated number of iterations. It can be seen that upon subsequent iterations, significant improvements are achieved in terms of both spatial range and perturbation intensities, compared to the result obtained with one iteration.

The previous results were obtained with the numerically simulated data directly. In order to evaluate the sensitivity of the proposed algorithm to noise in measurement data, we have also added random noise to calculated data. Figs. 5 and 6 show the reconstruction results at 5% noise level. The target profile is the same as shown in Figs. 3(a) and 4(a). Figs. 5(a) and 6(a) show the results obtained with the first-order Born approximation. Figs. 5(b) and 6(b) show the results after 20 iterations. Again, significant improvements have been obtained with additional iterations in terms of both spatial range and perturbation intensities. The reconstruction result after 20 iterations is satisfactory, but not as sharp as that obtained from noise-free data.

5. Discussion and Conclusion

We have derived the integral equation for the photon flux and its phase based on the diffusion equation, from which we derived the general Born-type inverse method for tissue optical image reconstruction. The Born-type iteration approach has been used for reconstruction of the absorption and diffusion coefficients in an inhomogeneous medium. It has been shown that this method can yield accurate reconstruction of absorption and diffusion coefficients from frequency domain data. The reconstruction results shown in Figs. 5-6 show that the algorithm can yield quantitatively (in terms of coefficient values) and qualitatively (in terms of location and shape) accurate reconstructions for both coefficients with about 20 iterations, for the test medium we have simulated. Obviously, the reconstruction results are more accurate, especially quantitatively, than the results obtained from only one iteration (i.e. Born approximation). In the simulations presented here, we have assumed that the background medium (*i.e.* the tissue at normal state without added tumors) is known precisely. In this case, we can reconstruct the "tumors" quite accurately. In practice, the true background medium will not be known precisely. Investigation of the sensitivity of the proposed algorithm to the variation of the background medium is a subject of our future studies.

Acknowledgement

This work was supported in part by the National Institutes of Health under Grant # RO1-CA59955, by an ONR grant # N000149510063, and by the New York State Science and Technology Foundation.

REFERENCES

[1] R. L. Barbour, H. L. Graber, R. Aronson and J. Lubowsky, "Model for 3-D Optical Imaging of Tissue," in *Proc. 10th Annual International Geoscience and Remote Sensing Symposium*, pp. 1395-1399, 1990.

[2] B. C. Wilson, E. M. Sevick, M. S. Patterson and B. Chance, "Time-Dependent Optical Spectroscopy and Imaging for Biomedical Applications," *Proceedings of the IEEE*, vol. 80, pp. 918-930, 1992.

[3] G. Muller, *ed.*, *Medical Optical Tomography: Functional Imaging and Monitoring*, (SPIE Press, Bellingham, Wash., 1993).

[4] E. Gratton, W. W. Mantulin, M. J. vandeVen, J. B. Fishkin, M. B. Maris and B. Chance, "A novel approach to laser tomography," Bioimaging, vol. 1, 40-46 (1993).

[5] M.A. O'Leary, D.A. Boas, B. Chance and A.G. Yodh, "Imaging of inhomogeneous turbid media using diffuse photon density waves," *In OSA Proceedings on Advances in Optical Imaging and Photon Migration*, R. R. Alfano, ed., pp. 106-115 (1994).

[6] A. Knuttel, J. M. Schmitt and J. R. Knutson, "Spatial localization of absorbing bodies by interfering diffusive photon-density waves," *Applied Optics*, vol. 32, pp. 381-389, 1993.

[7] B. W. Pogue and M. S. Patterson, "Forward and Inverse Calculations for 3-D Frequency-Domain Diffuse Optical Tomography," SPIE Proc., Vol. 2389, pp. 238-339, 1995.

[8] S. A. Arridge, M. Schweiger, M. Hiraoka, D. T. Delay, "A finite Element Approch for Modeling Photon transport in Tissue," *Med. Phys.*, 20(2), pp. 299-309, 1993.

[9] S. A. Arridge and M. Schweiger, "Near-infrared Imaging: Photon Measurement Density Functions," SPIE Proc., Vol. 2389, pp.366-377, 1995.

[10] H. Jiang, K. D. Paulsen and U. L. Osterberg, "Optical Image Reconstruction Using Frequency-Domain Data: Simulations and Experiments", *J. Opt. Soc. Am. A*, vol. 13 pp. 253-266, 1996.

[11] R. L. Barbour, H. L. Graber, J. Chang, S. L. S. Barbour, P. C. KOO, and R. Aronson, "MRI-Guided Optical Tomography: Prospects and Computation for a New Imaging Method," *IEEE Comp. Sci. & Eng.*, vol. 2, pp. 63-77, 1995.

[12] Y. Yao, Y. Wang, Y. Pei, W. Zhu, J. Hu and R. L. Barbour, "Frequency Domain Optical Tomography in Human Tissue," in *Experimental and Numerical Methods for Solcing Ill-Posed Inverse Problems: Medical and Nonmedical Applications*, SPIE Proc., Vol. 2570, pp. 254-266, 1995.

[13] Y. L. Pei, Y. Q. Yao, F. B. Lin, Y. Wang, and R. L. Barbour, "A New Finite Element Approach for Optical Tomography," *Proc. Spectroscopy and Imaging in Scattering Media*, in *80th Anniversary OSA Annual Meeting & Exhibit*, Rochester, NY, 1996.

[14] Y. Yao, *Forward and Inverse Studies for Optical Image Reconstruction*, Ph. D. Dissertation, Polytechnic University, May, 1996.

[15] R. C. Gonzalez and R. E. Woods, *Spatial Digital Image Processing*, Addison-Wesley, 1992.

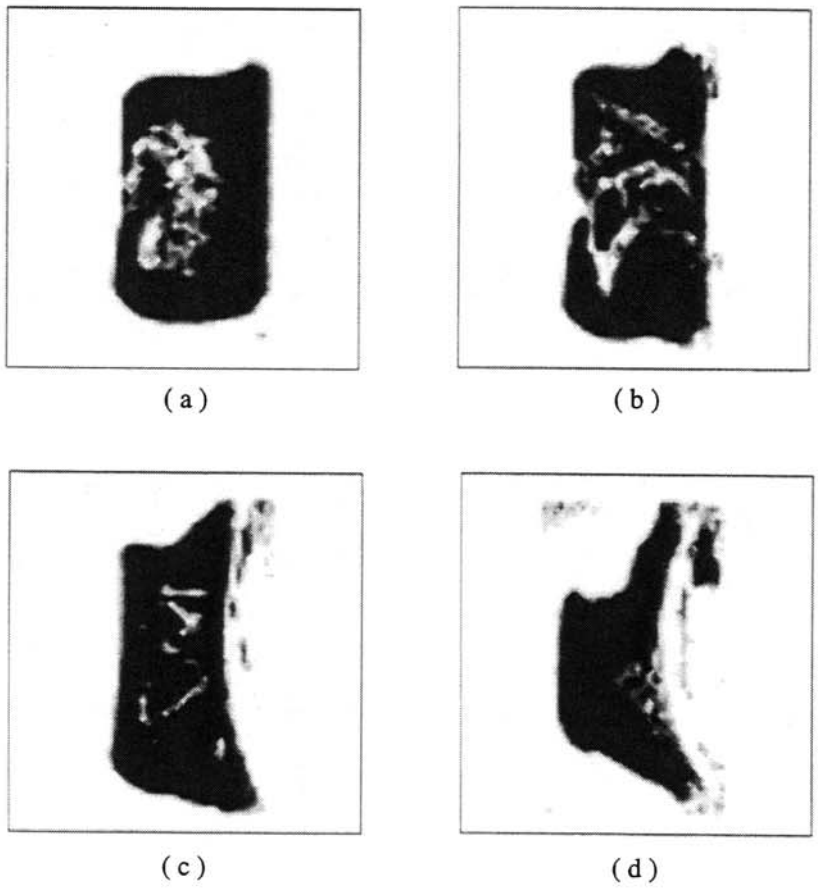

Figure 1: Sagittal cuts of a MR breast scan: (a) 5^{th} (b) 10^{th} (c) 15^{th} and (d) 20^{th} slices.

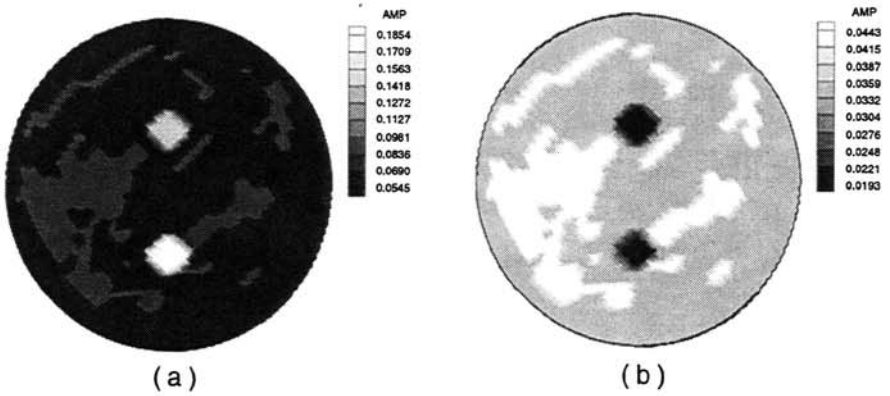

Figure 2: The distribution of the absorption (a) and diffusion (b) coefficients in an axial slice derived from the MRdata. Two "pathologies" are added to the background medium.

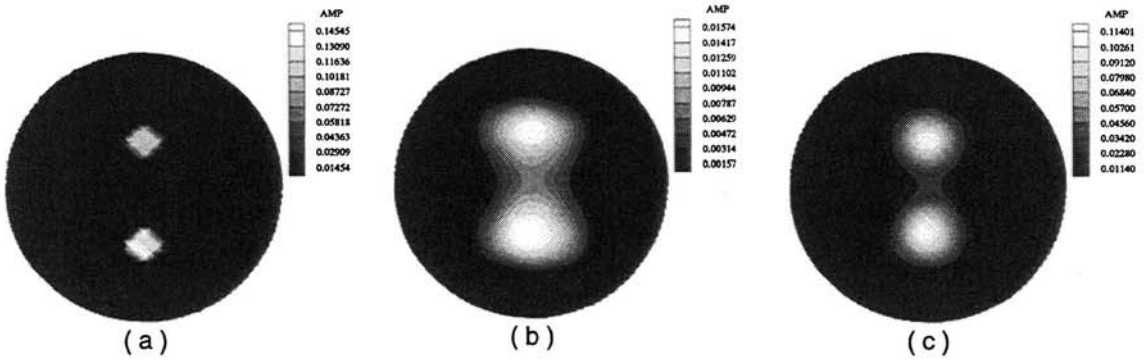

Figure 3: Reconstructed absorption distribution (only perturbation from the background medium is shown) from noise-free simulated data. (a) is the image of the true perturbation; (b) is the reconstructed image after 1 iteration (*i.e.*, Born approximation); and (c) is the reconstructed image after 20 iterations. The modulation frequency is 200 MHz.

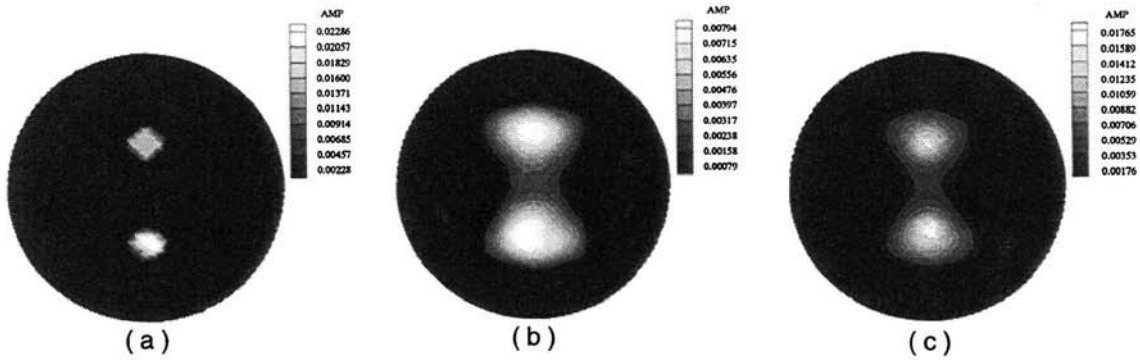

Figure 4: Reconstructed diffusion coefficients. (a) is the image of the true perturbation; (b) is the reconstructed image after 1 iteration; and (c) is the reconstructed image after 20 iterations. The modulation frequency is 200 MHz.

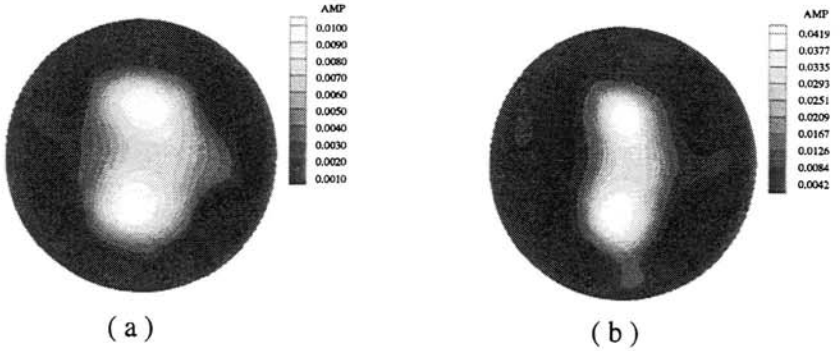

(a) (b)

Figure 5: Reconstructed absorption distribution (only perturbation from the background medium is shown) from simulated data with 5% noise. (a) is the reconstructed image after 1 iteration (*i.e.*, Born approximation); and (b) is the reconstructed image after 20 iterations. The modulation frequency is 200 MHz.

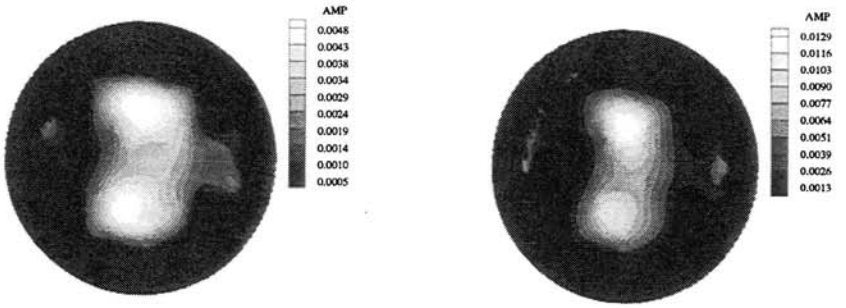

(a) (b)

Figure 6: Reconstructed diffusion coefficients from simulated data with 5% noise. (a) is the reconstructed image after 1 iteration; and (b) is the reconstructed image after 20 iterations. The modulation frequency is 200 MHz.